AGU PUBLICATIONS

JGR

Journal of Geophysical Research: Planets

RESEARCH ARTICLE
10.1002/2015JE004881

This article is a companion to *Thorpe et al.* [2015] doi:10.1002/2015JE004863.

Key Points:
- Nonlinear relationship between known and modeled abundance for TIR spectra of fine-grained mixtures
- Partial least squares is able to recover the known abundances for synthetic mixtures and mudstones
- PLS can be used to recover abundances of fine-grained rocks from planetary TIR observations

Supporting Information:
- Text S1 and Figures S1–S18
- Table S1
- Table S2
- Table S3
- Table S4
- Table S5

Correspondence to:
C. Pan,
pancong419@gmail.com

Citation:
Pan, C., A. D. Rogers, and M. T. Thorpe (2015), Quantitative compositional analysis of sedimentary materials using thermal emission spectroscopy: 2. Application to compacted fine-grained mineral mixtures and assessment of applicability of partial least squares methods, *J. Geophys. Res. Planets*, *120*, 1984–2001, doi:10.1002/2015JE004881.

Received 29 JUN 2015
Accepted 29 OCT 2015
Accepted article online 2 NOV 2015
Published online 26 NOV 2015

Quantitative compositional analysis of sedimentary materials using thermal emission spectroscopy: 2. Application to compacted fine-grained mineral mixtures and assessment of applicability of partial least squares methods

C. Pan[1], A. D. Rogers[1], and M. T. Thorpe[1]

[1]Department of Geosciences, Stony Brook University, Stony Brook, New York, USA

Abstract Fine-grained sedimentary deposits on planetary surfaces require quantitative assessment of mineral abundances in order to better understand the environments in which they formed. One way that planetary surface mineralogy is commonly assessed is through thermal emission (~6–50 μm) spectroscopy. To that end, we characterized the TIR spectral properties of compacted, very fine-grained mineral mixtures of oligoclase, augite, calcite, montmorillonite, and gypsum. Nonnegative linear least squares minimization (NNLS) is used to assess the linearity of spectral combination. A partial least squares (PLS) method is also applied to emission spectra of fine-grained synthetic mixtures and natural mudstones to assess its applicability to fine-grained rocks. The NNLS modeled abundances for all five minerals investigated are within ±10% of the known abundances for 39% of the mixtures, showing the relationships between known and modeled abundance follow nonlinear curves. The poor performance of NNLS is due to photon transmission through small grains over portions of the wavelength range and multiple reflections in the volume. The PLS method was able to accurately recover the known abundances (to within ±10%) for 78–90% of synthetic mixtures and for 85% of the mudstone samples chosen for this study. The excellent agreement between known and modeled abundances is likely due to high absorption coefficients over portions of the thermal infrared (TIR) spectral range, and thus, combinations are linear over portions of the range. PLS can be used to recover abundances from very fine-grained rocks from TIR measurements and could potentially be applied to landed or orbital TIR observations.

1. Introduction

Sedimentary deposits, including fine-grained siliciclastic materials, clay, sulfate, and hematite, have been found on the Martian surface, and their formation may indicate liquid water activity for a period of time in early Martian history (e.g., [*Christensen et al.*, 2000a; *Malin and Edgett*, 2000; *Squyres et al.*, 2004; *Ehlmann et al.*, 2008b; *Grotzinger et al.*, 2014; *McLennan et al.*, 2014]). For example, sandstones in the Burns formation, Meridiani Planum, contain significant abundances of sulfate and hematite, indicating possible evaporitic and diagenetic processes [e.g., *Christensen et al.*, 2004b; *McLennan et al.*, 2005; *Glotch et al.*, 2006]. Carbonate minerals are identified in the soils at the Mars Phoenix Landing site [*Boynton et al.*, 2009], in rare outcrops [*Ehlmann et al.*, 2008a, 2008b], and in low quantities in the global Martian dust [*Bandfield et al.*, 2003]. Last, clay minerals have been identified in numerous geologic settings [e.g., *Poulet et al.*, 2005; *Ehlmann et al.*, 2011; *Carter et al.*, 2013], including in fans and deltas within sedimentary basins, which may indicate alteration by substantial amounts of water.

Interpreting the origin of sedimentary materials requires detailed analysis of geologic context, stratigraphy, mineral assemblages, and mineral abundances (e.g., [*McLennan et al.*, 2005; *Tornabene et al.*, 2008; *Wray et al.*, 2008; *Mustard et al.*, 2009; *Dobrea et al.*, 2010; *Michalski and Niles*, 2010; *Roach et al.*, 2010; *Ehlmann et al.*, 2011; *Grotzinger and Milliken*, 2012]). One of the ways to characterize mineral assemblage and abundances remotely is through thermal emission spectral measurements (e.g., [*Lyon*, 1965; *Kahle et al.*, 1984; *Christensen et al.*, 2000b; *Lucey*, 2004; *Hook et al.*, 2005]), which have been acquired of Martian surfaces both from orbit and from the Mars Exploration Rover missions. Data from the Mars Global Surveyor Thermal Emission Spectrometer [*Christensen et al.*, 2001] (200–1650 cm^{-1}, 3 × 8 km spatial resolution) have been used to determine the distribution and abundance of minerals at global and regional scales. Miniature Thermal Emission

Spectrometers [*Christensen et al*., 2004a, 2004b], on board the Spirit and Opportunity rovers, measured thermally emitted radiance from soils, outcrops, and float rocks over the 400–1650 cm^{-1} range. And the Mars Odyssey Thermal Emission Imaging System [*Christensen et al*., 2003] measures emitted energy over nine broad spectral channels between ~650 and 1550 cm^{-1}, with a spatial resolution of 100 m/pixel, allowing for discrimination of compositional units at the outcrop scale.

Spectral absorptions measured in the thermal infrared (TIR) range arise from molecular vibrations in the material of interest. The vibrations occur at specific frequencies based on the chemical composition and structure of the mineral of interest (e.g., [*Farmer*, 1974]). For mineral mixtures (e.g., rocks), the spectra of the individual components of the rock combine to produce the mixed spectrum. Previous studies of igneous and metamorphic rocks, as well as coarse-grained sand mixtures, have shown that the component spectra combine in proportion to their volume abundance in the mixed spectrum when grains are larger than $\sim > 60\,\mu m$ [*Ramsey and Christensen*, 1998; *Feely and Christensen*, 1999]. On this basis, linear spectral models of thermal emission spectra measured remotely have been used to estimate mineral abundances of Martian surface materials in low-dust regions [e.g., *Bandfield*, 2002; *Rogers and Christensen*, 2007; *Huang and Xiao*, 2014]. However, the spectral mixing behavior of compacted, fine-grained mineral mixtures that would be characteristic of sedimentary depositional environments (e.g., paleosols, mudstones, mixed-phase cements) has received little attention.

A difference in spectral mixing behavior for fine-grained rocks might be expected, given previous work demonstrating spectral dependence on grain size and porosity in the thermal infrared (TIR) (e.g., [*Hunt and Vincent*, 1968; *Clark and Roush*, 1984; *Salisbury and Wald*, 1992; *Hapke*, 1993; *Mustard and Hays*, 1997]. In a noncompacted volume consisting of particles whose diameters are on the order of the measured wavelength, there are proportionally more surface and internal reflections compared to larger grains. In spectral regions where the absorption index (k) is large (strongly absorbing), a reduction in spectral contrast with decreasing particle size is observed due to increased opportunities for absorption. In spectral regions where k is small (weakly absorbing), spectral contrast increases, due to increased opportunity for photons to exit the surface through refraction at each grain interface [*Hunt and Vincent*, 1968; *Moersch and Christensen*, 1995]. For mixtures of noncompacted particles whose diameters are on the order of the measured wavelength, the increased number of reflections described above leads to photon interaction with multiple phases before exiting the mixture, and thus, the observed absorptions are not predictive of volume abundances (nonlinear mixing) (e.g., [*Mustard and Hays*, 1997; *Ramsey and Christensen*, 1998]).

In a volume where small particles are closely packed, multiple surface reflections are reduced, and spectra more closely resemble those from coarse-grained materials [*Salisbury and Wald*, 1992]. Despite this, a volume scattering component remains due to the grain size being equal to or smaller than the mean optical path length (e.g., [*Hunt and Logan*, 1972; *Clark and Roush*, 1984]). These effects of compaction on fine-grained *mixtures* have not been examined in a systematic manner, however. Because k is wavelength-dependent for each mineral, and transmission through small grains occurs where k is small (e.g., [*Hunt and Logan*, 1972; *Salisbury et al*., 1987; *Cooper and Mustard*, 2002]), we would expect a mixture of linear and nonlinear mixing behavior that varies with wavelength. Characterizing the TIR spectral mixing behavior of compacted fine-grained mineral assemblages is necessary for facilitating quantitative mineralogy of sedimentary surfaces and understanding their origins from spectral measurements.

In a companion paper [*Thorpe et al*., 2015, hereafter as "paper 1"], we characterize the spectral mixing behavior of a suite of terrestrial sandstones and mudstones to assess the accuracy of quantitative mineral abundance estimates derived from thermal emission spectra of sedimentary rocks. In this paper, we characterize the spectral properties of compacted, very fine grained ($<$10–25 μm) mineral mixtures to assess spectral mixing behavior of very fine grained materials. For the first time, we also apply a partial least squares (PLS) method to model mineral abundance from thermal emission spectra and provide an assessment of the applicability of PLS to fine-grained rocks.

2. Data and Methods

2.1. Sample Preparation

Five minerals including oligoclase, augite, calcite, gypsum, and montmorillonite were used for this study. These five minerals were chosen to encompass a suite of basaltic minerals as well as alteration products that

Table 1. Percentile of Particle Size[a]

	10th Percentile	20th Percentile	50th Percentile	80th Percentile	90th Percentile
Oligoclase	0.9 μm	1.4 μm	2.9 μm	5.5 μm	7.8 μm
Augite	0.8 μm	1.7 μm	4.1 μm	7.3 μm	9.4 μm
Calcite	0.9 μm	1.3 μm	2.5 μm	4.9 μm	7.5 μm
Gypsum	4.8 μm	10.0 μm	23.7 μm	45.1 μm	62.2 μm
Montmorillonite	0.9 μm	1.4 μm	2.8 μm	6.6 μm	17.9 μm

[a]Oligoclase (WAR-0234), Augite (WAR-6474), Calcite (WAR-1604), Montmorillonite (SWy-1), and Gypsum (CAS-10101414). The median grain size of montmorillonite, derived from laser diffraction, is larger than expected for pure clay. This may be due to either particle flocculation during measurement [*Sperazza et al.*, 2004] or possibly larger-grained impurities [*Chipera and Bish*, 2001]. Oligoclase and augite compositions were confirmed with electron microprobe. Calcite and gypsum samples are spectrally indistinguishable from well-characterized samples in *Lane and Christensen* [1997] and *Lane* [2007], confirming the quality of these samples. The montmorillonite sample was characterized using X-ray diffraction and contains ~6% quartz. No other impurities were detected.

have been identified on Mars. Montmorillonite was purchased from the Clay Minerals Society, and the other four were from Ward's Science. The oligoclase sample from Ward's was labeled "albite" but is actually oligoclase, confirmed by electron microprobe (Table 1). The gypsum sample was already in powdered form. The oligoclase, augite, and calcite samples were crushed with an agate mortar and pestle. Except for gypsum, all samples were then centrifuged to obtain particle sizes less than 10 μm [*Jackson*, 1967] and to reduce impurities for montmorillonite [*Moore and Reynolds*, 1997] (Table 1). Particle size was measured using a Malvern Instruments Mastersizer 2000 laser diffractometer with Hydro 2000MU pump accessory at Stony Brook University. The median particle sizes used in this study were 3 μm for oligoclase, 3 μm for montmorillonite, 4 μm for augite, 2.5 μm for calcite, and 23 μm for gypsum (Table 1). Mixtures of two, three, and four components were made in varying proportions by volume (Table 2). Single phase and mixture samples were pressed into ~3 mm thick pellets with ~1 cm in diameter at 15000 pound-force per square inch to generate compacted samples. Pellets were visually shiny and reflective, suggesting an absence of clinging fines. Though pressing can result in a preferred grain orientation, this should not negatively influence our results because we are using pressed pellets for both the mixed spectra and the end-member spectra, and thus, orientations should be similar. Coarse-grained samples with particle size larger than 500 μm of oligoclase, augite and calcite, and loose powder of all five minerals were also prepared for spectroscopic measurements and comparison.

2.2. Raman Microspectroscopy

To validate whether the targeted volume percentages in Table 2 are close to areal abundance in the pellets, Raman spectral images of some mixture pellets were measured. The Raman spectra were measured using a WITec alpha300R confocal Raman imaging system at the Stony Brook University Vibrational Spectroscopy

Table 2. Volume Abundance of Mixture Minerals

Mixtures	Proportion (vol %)
Oligoclase:augite	10:90, 20:80, 50:50, 80:20, 90:10
Oligoclase:montmorillonite	10:90, 20:80, 50:50, 80:20, 90:10
Oligoclase:gypsum	10:90, 20:80, 50:50, 80:20, 90:10
Augite:montmorillonite	10:90, 20:80, 50:50, 80:20, 90:10
Augite:calcite	10:90, 20:80, 50:50, 80:20, 90:10
Augite:gypsum	10:90, 20:80, 50:50, 80:20, 90:10
Montmorillonite:calcite	10:90, 20:80, 50:50, 80:20, 90:10
Montmorillonite:gypsum	10:90, 20:80, 50:50, 80:20, 90:10
Calcite:gypsum	10:90, 20:80, 50:50, 80:20, 90:10
Oligoclase:augite:calcite	20:20:60, 40:40:20, 45:45:10
Oligoclase:augite:montmorillonite	20:20:60, 40:40:20, 45:45:10
Oligoclase:augite:gypsum	20:20:60, 40:40:20, 45:45:10
Oligoclase:montmorillonite:gypsum	80:10:10, 60:20:20, 20:40:40
Augite:montmorillonite:gypsum	80:10:10, 60:20:20, 20:40:40
Oligoclasemontmorillonite:calcite	80:10:10, 60:20:20, 20:40:40
Augite:montmorillonite:calcite	80:10:10, 60:20:20, 20:40:40
Oligoclase:augite:montmorillonite:calcite	40:40:10:10, 30:30:20:20
Oligoclase:augite:montmorillonite:gypsum	40:40:10:10, 30:30:20:20

Lab. For each pellet, hyperspectral Raman images of three 75×75 μm areas were measured for three different pellets with 1 cm^{-1} spectral resolution. The spectral angle mapping (SAM) [*Kruse et al*., 1993] supervised classification method was used to determine the areal abundance of minerals in each area. SAM analysis of Raman spectral images results showed that areal abundance is within ±5% of targeted volume percentage in these pellets. An example is shown in the supporting information (Figure S16).

2.3. Thermal Infrared Spectroscopic Measurements

Thermal infrared spectra of pellets were measured at the Stony Brook University Vibrational Spectroscopy Lab from ~225 to 2000 cm^{-1} at 2 cm^{-1} spectral sampling using a Nicolet 6700 Fourier transform infrared spectrometer. Except for gypsum-bearing samples, samples were heated and maintained at 80°C to provide adequate signal-to-noise ratio. In order to avoid dehydration of gypsum during measurement, gypsum-bearing mixtures were cooled with dry ice for several hours and then measured [*Baldridge and Christensen*, 2009]. Sample temperatures during measurement were ~ −10°C, ~35°C below detector temperature. This results in slightly lower signal-to-noise ratios than the conventional emissivity measurement method (where samples are heated, e.g., *Ruff et al*. [1997]), but because the samples for measurement exhibit high spectral contrast, the quality of the measured spectra is more than sufficient for resolving all features [*Baldridge and Christensen*, 2009]. A blackbody heated to 70°C and 100°C was used to generate the instrument response function, which is then use to convert measured sample signal to radiance units. Environmental radiance contributions are controlled using a temperature-regulated sample chamber; these contributions are mathematically removed from the measured radiance using the methods of *Ruff et al*. [1997].

2.4. Nonnegative Linear Least Squares Minimization

To assess linearity of spectral combination in compacted fine-grained mixtures, nonnegative linear least squares minimization (NNLS) [*Lawson and Hanson*, 1974] using spectra of pellets and powders of the end-member minerals (Table 1) was used to model mineral abundance of mixtures over the 350–1650 cm^{-1} spectral range. Most of the major and minor minerals found on the Martian surface have thermal infrared absorption features in these spectral ranges, and the range is comparable to that of the Mars Global Surveyor TES and Mars Exploration Rover Mini-TES instruments. Linear least squares minimization has been widely used to derive surface emissivity and mineral abundance from TES and Mini-TES data (e.g., [*Smith et al*., 2000; *Bandfield*, 2002; *Glotch et al*., 2006; *Ruff et al*., 2006; *Rogers and Christensen*, 2007; *Koeppen and Hamilton*, 2008; *Rogers and Aharonson*, 2008; *Ruff et al*., 2011; *Hamilton and Ruff*, 2012; *Pan et al*., 2015]. The use of this method assumes linear spectral mixing across the entire spectral range (section 1).

2.5. Partial Least Squares

Partial least squares (PLS) is an extension of a multiple linear regression statistical method that assumes a system of observations can be described with a small number of unobservable (or "latent") variables, similar to principal component or factor analysis techniques. PLS generalizes predictive models from these latent variables [*Wold*, 1982; *Wold et al*., 2001] and is widely used in chemometrics, bioinformatics, and related fields. For example, it is one of the primary data reduction techniques employed by the Mars Science Laboratory Rover Curiosity ChemCam team [*Clegg et al*., 2009; *Dyar et al*., 2012]. It has been successfully applied to thermal reflectance spectra of granites [*Hecker et al*., 2012] and was also investigated as a possible technique to retrieve mineral abundance from near-infrared spectra of mineral mixtures [*Li et al*., 2012] (discussed further in section 4.3). PLS analysis [*Wold*, 1982] was employed to generate a calibration model from which unknown mineral abundance of mixture spectra (testing data set) can be predicted using spectra with known mineral abundance (training data set). Both NNLS and PLS involve generating regression models to solve the linear multivariate problem:

$$Y = \beta_0 + \beta_1 X_1 + \beta_2 X_2 + \cdots + \beta_n X_n$$

where Y is one or several dependent variables, X is the independent variable or predictor variable, β_0 is the regression coefficient for the intercept, and $\beta_i (i = 1 \ldots n)$ is the matrix of regression coefficients. For NNLS, Y is the mixture spectrum, X_i is the spectral library (usually consisting of well-characterized, "pure" mineral sample spectra) [*Lawson and Hanson*, 1974; *Ramsey and Christensen*, 1998], and β_i is a function of the number of library spectra. For PLS, X_i is a matrix containing the emissivity spectra of mixtures with known abundances, where i is the number of spectral channels, Y is the corresponding matrix of known mineral abundances (vol %), and β_i is the regression coefficient for each spectral channel i. PLS analysis determines

Table 3. Mineral Abundance From XRD and Modeled Abundance Derived From PLS and NNLS for Mudstones[a]

Sample Label	Mineral Abundance From XRD				PLS Modeled Abundance				NNLS Modeled Abundance			
	Feldspar	Quartz	Clay	Mica	Feldspar	Quartz	Clay	Mica	Feldspar	Quartz	Clay	Mica
sm-75-165	47.13	12.17	4.34	0.00	39.02	20.95	23.79	14.22	47.13	12.17	4.34	0.00
sm-75-103	21.26	14.84	12.08	3.25	29.55	25.32	14.73	28.81	21.26	14.84	12.08	3.25
sm-75-104	20.21	9.02	15.62	2.57	18.11	23.18	19.35	36.53	20.21	9.02	15.62	2.57
sm-75-105	51.01	12.30	5.13	0.00	51.72	19.11	16.98	10.19	51.01	12.30	5.13	0.00
sm-75-107	35.35	2.27	6.23	0.00	56.62	9.04	11.16	22.42	35.35	2.27	6.23	0.00
sm-75-134	28.67	33.45	13.50	5.27	24.03	38.31	12.47	24.92	28.67	33.45	13.50	5.27
sm-75-140	24.40	22.89	14.45	3.91	16.56	38.51	11.17	34.04	24.40	22.89	14.45	3.91
sm-75-158	12.64	18.17	3.52	0.00	44.59	37.03	31.21	0.00	12.64	18.17	3.52	0.00
sm-75-113	16.25	29.25	13.19	5.62	17.98	39.47	11.02	30.84	16.25	29.25	13.19	5.62
sm-75-120	7.10	29.41	11.18	11.47	7.33	35.35	9.27	47.89	7.10	29.41	11.18	11.47
sm-75-142	10.83	15.98	16.26	12.33	10.99	30.37	8.25	50.61	10.83	15.98	16.26	12.33
sm-75-115	15.15	23.53	10.86	12.07	18.99	26.43	21.12	32.68	15.15	23.53	10.86	12.07
sm-75-117	13.44	47.69	7.84	4.04	14.41	42.92	9.61	31.99	13.44	47.69	7.84	4.04
sm-75-123	24.29	17.90	12.22	10.06	14.61	24.38	15.42	44.58	24.29	17.90	12.22	10.06

[a]Mineral abundance is determined by full pattern X-ray diffraction quantitative refinements from *Thorpe et al*. [2015].

the statistical linear correlation between the known mineral abundance and observed spectra (both of these constitute the training set).

Single-phase pellets and powders and all of the mixtures from Table 2 were used as the training data set for PLS, and based on this training set, regression coefficients were derived for each mineral. The derived regression coefficients vary as a function of wavelength and are related to the thermal infrared spectral features that most strongly drive the correlations between mineral abundance and spectral properties in the mixed set of spectra. This is described in more detail in section 3.1.2. The "PLS-2" method commonly applied to ChemCam data [*Clegg et al*., 2009; *Dyar et al*., 2012], where multiple *Y* variables are simultaneously analyzed, was used. PLS-2 allows for better prediction of regression coefficients over PLS-1, because of correlations between mineral components within the mixtures (e.g., as one component is increased, there must be a decrease in another component) [e.g., *Dyar et al*., 2012]. In this work, the number of latent variables within the training set was estimated by examining the percentage of variance explained in the response variable *Y* as a function of the number of components (Figures S17 and S18). Higher-number components correspond with smaller contribution to total variance. The number of components chosen for our predictive models for the compacted fine-grained mixtures was 15, based on an iterative process of examining the percent of variance contribution and checking the modeled abundance results for changes with increasing number of components. Using higher numbers of components beyond 15 was found to have little effect on the predictive performance of the model ($<$3% change in modeled abundance, on average); these first 15 components account for $>$90% of the variance within the training set. Next, a "leave-one-out" approach was used to generate regression coefficients from the original training data set, excluding one spectrum from the set. Those coefficients were then applied to the excluded spectrum to retrieve mineral abundance for that spectrum. This process was repeated for all of the mixtures from Table 2 and then compared with the known abundances for each mixture to evaluate the PLS model accuracy.

Lastly, we applied the same method to the mudstone samples from paper 1 with the same wave number range as paper 1 (230–1650 cm^{-1}), in order to examine the performance of PLS applied to natural rock samples. There are 14 mudstone samples, whose mineral abundances were determined by X-ray diffraction (XRD) [*Thorpe et al*., 2015] (given also in Table 3). The mudstone samples are from the Huronian Supergroup (2.5–2.2 Ga) outcrop belt on the northern shore of Lake Huron, Canada. As described in paper 1, they vary in their abundances of sericite, chlorite, and framework minerals. Only the minerals with abundances more than 3 vol %, as determined by XRD, and minerals that were clearly present in almost all of the mudstone samples were included as inputs to our PLS model. These minerals groups are feldspar, quartz, clays, and mica. Thus, the training set for the mudstone samples consists of the XRD-determined abundances for each of these four groups, as well as the mudstone spectra. The number of components chosen for mudstone models was five (Figure S18), which represents more than 95% of the variance. Using higher numbers of components had negligible effects on the final modeled abundances.

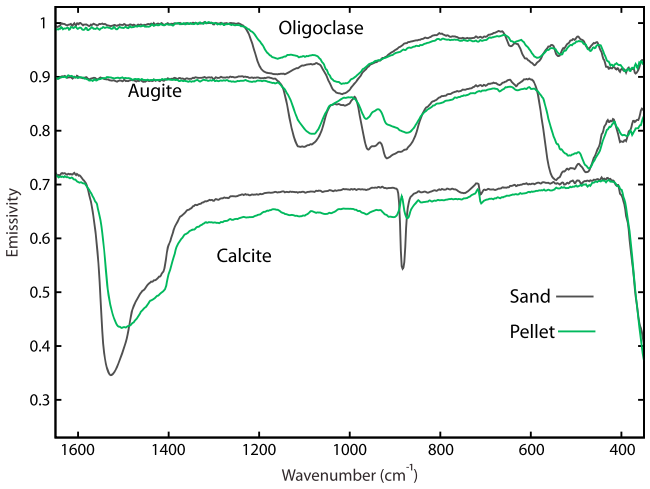

Figure 1. Spectral comparison of sand (500–841 μm) and pellet samples of oligoclase, augite, and calcite. Spectral pairs are offset for clarity. No scaling factors were applied.

3. Results

3.1. Sand Samples and Pressed Pellets

Figure 1 shows a comparison of TIR spectra of sand (500–841 μm) and pellet samples of oligoclase, augite, and calcite. Notable differences between the sand and pellet versions of each mineral are present, both in terms of spectral contrast and spectral shape. These differences likely arise from an increased contribution of volume scattering in the compacted fine-grained material relative to that in the larger, optically thick sand grains.

3.1.1. NNLS

In this section, we present the spectra from each set of mineral mixtures (Table 2), along with the best-fit spectral model from NNLS (Figures 2–4). Due to space limitations, only one representative set of spectra from the binary, ternary, and quarternary mixtures is shown. The remaining sets of spectra are shown in the supporting information (Figures S1–S15). In Figure 5, we show the modeled abundances for all mixtures, compared with the known abundance.

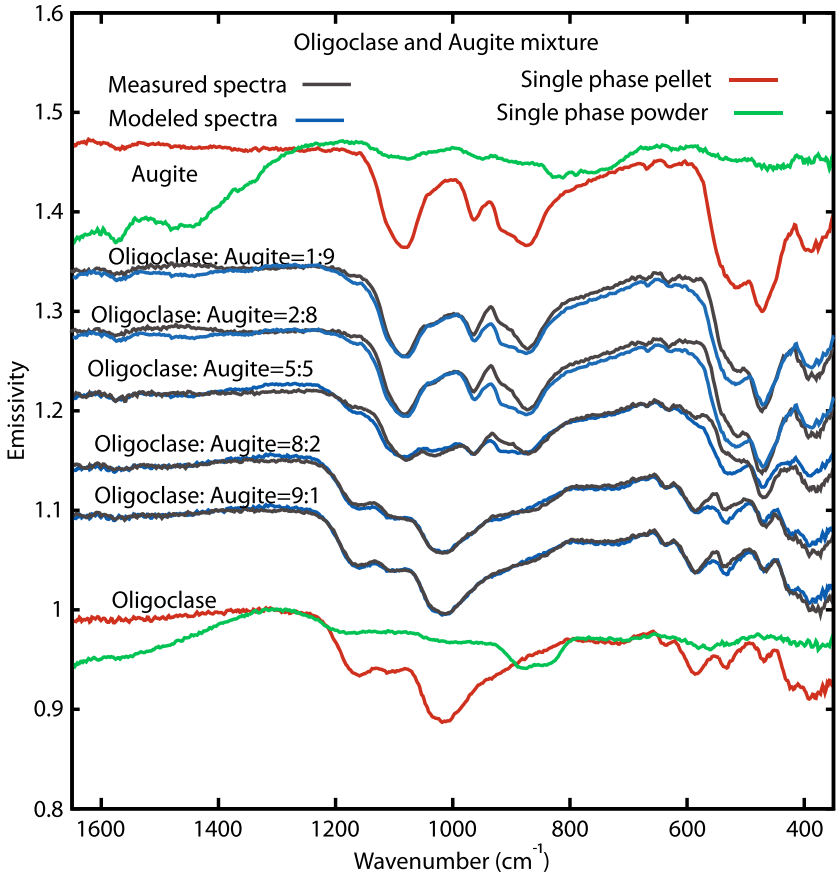

Figure 2. Measured and modeled spectra of oligoclase and augite compacted mixtures derived from NNLS. The mixtures were modeled with compacted oligoclase and compacted augite only. Both pellet and powder spectra of single-phase end-members were plotted for comparison. Spectral pairs are offset for clarity. No scaling factors were applied.

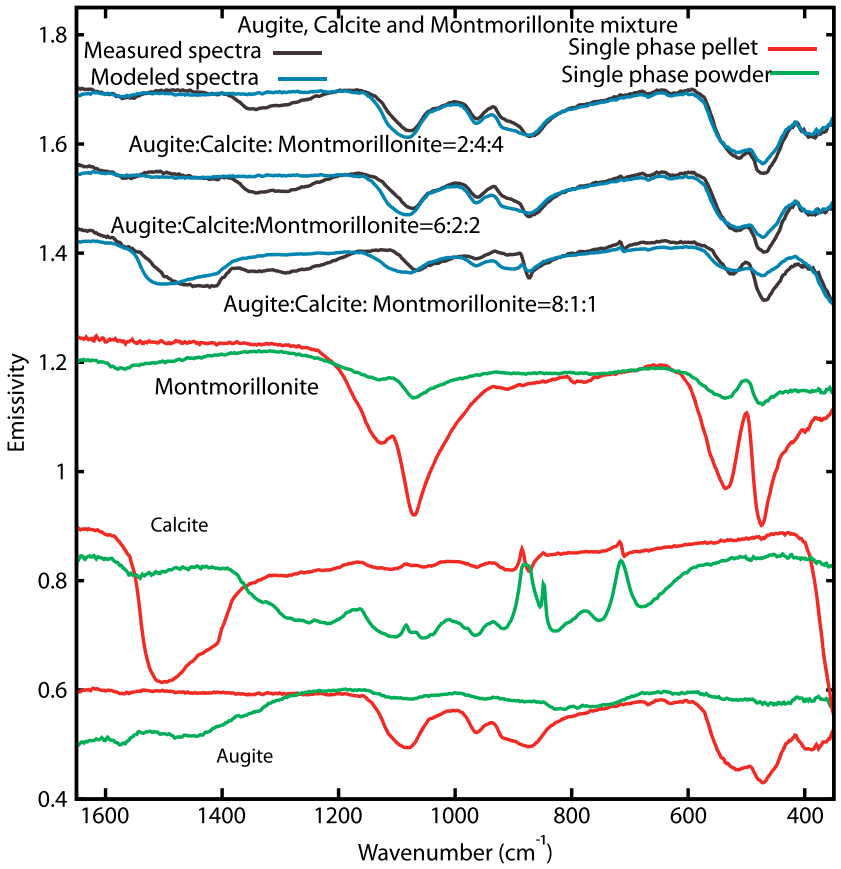

Figure 3. Measured and modeled spectra of augite, calcite, and montmorillonite compacted mixtures from NNLS. The mixtures were modeled with compacted augite, calcite, and montmorillonite only. Both pellet and powder spectra of single-phase end-members were plotted for comparison. Spectra are offset for clarity. No scaling factors were applied.

Figures 2–4 show representative model fits from 3 of the 18 mixtures examined. Some of the mixtures are well modeled by their end-member pellet components, whereas others are not. Additionally, some spectra are well modeled over portions of the spectral range, with other portions showing large misfits. Because each spectrum was modeled with its known components, the possibility of missing end-members may be ruled out, and the misfits may be attributed directly to nonlinear spectral mixing.

For oligoclase-bearing mixtures, approximately 60% of modeled oligoclase abundances fall within ±10% of the true abundance, with remaining mixtures generally overestimated. Model accuracy was generally better for two component mixtures than for more complex mixtures with three or more components (Figure 5a). Modeled abundance accuracy is generally better for higher true abundances of oligoclase.

For augite-bearing mixtures, approximately half of the results fall within ±10% of the true abundance, with the remaining half generally overestimated (Figure 5b). There is no clear trend of the model accuracy with mixture complexity or true abundance.

Approximately 60% of the modeled calcite abundances are within ±10% of true abundance, whereas the remainder is generally overestimated (Figure 5c). For the three- and four-component mixtures, smaller abundances (<20%) are more accurately modeled.

For montmorillonite-bearing mixtures, ~30% of the results fall within 10% from the known, with most modeled abundances underestimated (Figure 5d). The modeled abundance accuracy improves when the true abundance of montmorillonite is less than 10%.

For gypsum-bearing mixtures, less than 40% of the results are within 10% of the known abundance (Figure 5e). The model accuracy improves slightly for lower abundances.

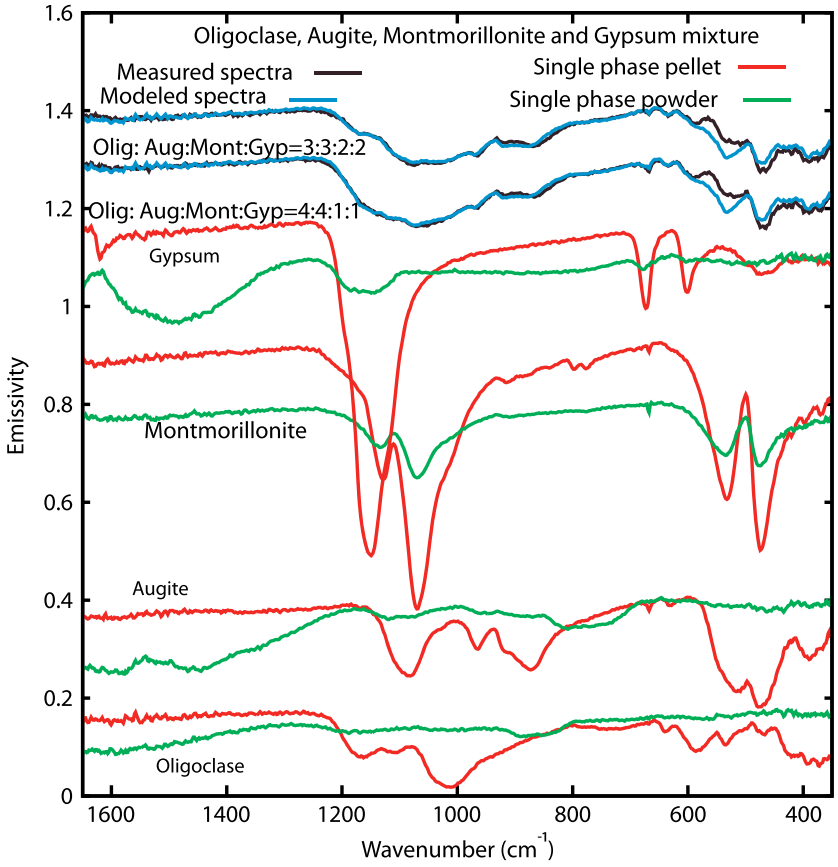

Figure 4. Measured and modeled spectra of oligoclase, augite, montmorillonite, and gypsum compacted mixtures from NNLS. Spectra of single phases were plotted for comparison. Spectral pairs are offset for clarity. No scaling factors were applied.

In summary, modeled abundances for all five minerals investigated are within ±10% of the known abundances for 39% of the mixtures. Model accuracy varies for each mineral group and also depends on what other mixture components are present. For example, montmorillonite abundances in binary mixtures with gypsum are accurately determined, whereas montmorillonite abundances in binary mixtures with augite are generally underestimated. For each mixture in a given series (e.g., 10:90, 20:80, and 50:50), differences from the known abundance generally do not follow a constant offset from the known, rather the relationships between known and modeled abundance follow nonlinear curves (Figure 5).

3.1.2. PLS

In this section, we present the regression coefficients derived from PLS using a training set containing all mixture series shown in Table 2, along with the end-members in both powder and pellet form (Figure 6). The inclusion of both powder and pellet end-member spectra in our training set allows us to better account for possible volume scattering features that are not fully diminished in spectra from the pelletized mixtures (section 1). The training set included 88 spectra in total. Then, using a leave-one-out approach, we repeatedly generate new sets of regression coefficients and then apply those to the missing sample (section 2.5), in order to determine the accuracy to which PLS can predict the mixture abundances (Figure 7).

For oligoclase, the strongest regression coefficients from PLS are located at ~1170, 870, 850, and between 750 and 790 cm^{-1} (Figure 6a). Of these, only the features near ~850 and 870 cm^{-1} correspond directly with the center of a major absorption (in this case, the powdered version of oligoclase). The regression coefficient peak near ~1170 cm^{-1} corresponds with the shoulder of the broad fundamental absorption in oligoclase, rather than the center of the absorption, and the strong coefficients between 750 and 790 cm^{-1} do not appear to correspond with any particular absorption in the pellet or powder versions of these samples. Pelletized oligoclase exhibits a deep absorption near ~1010 cm^{-1}, which corresponds with a moderately strong negative regression coefficient "dip" but this feature is not as strongly predictive

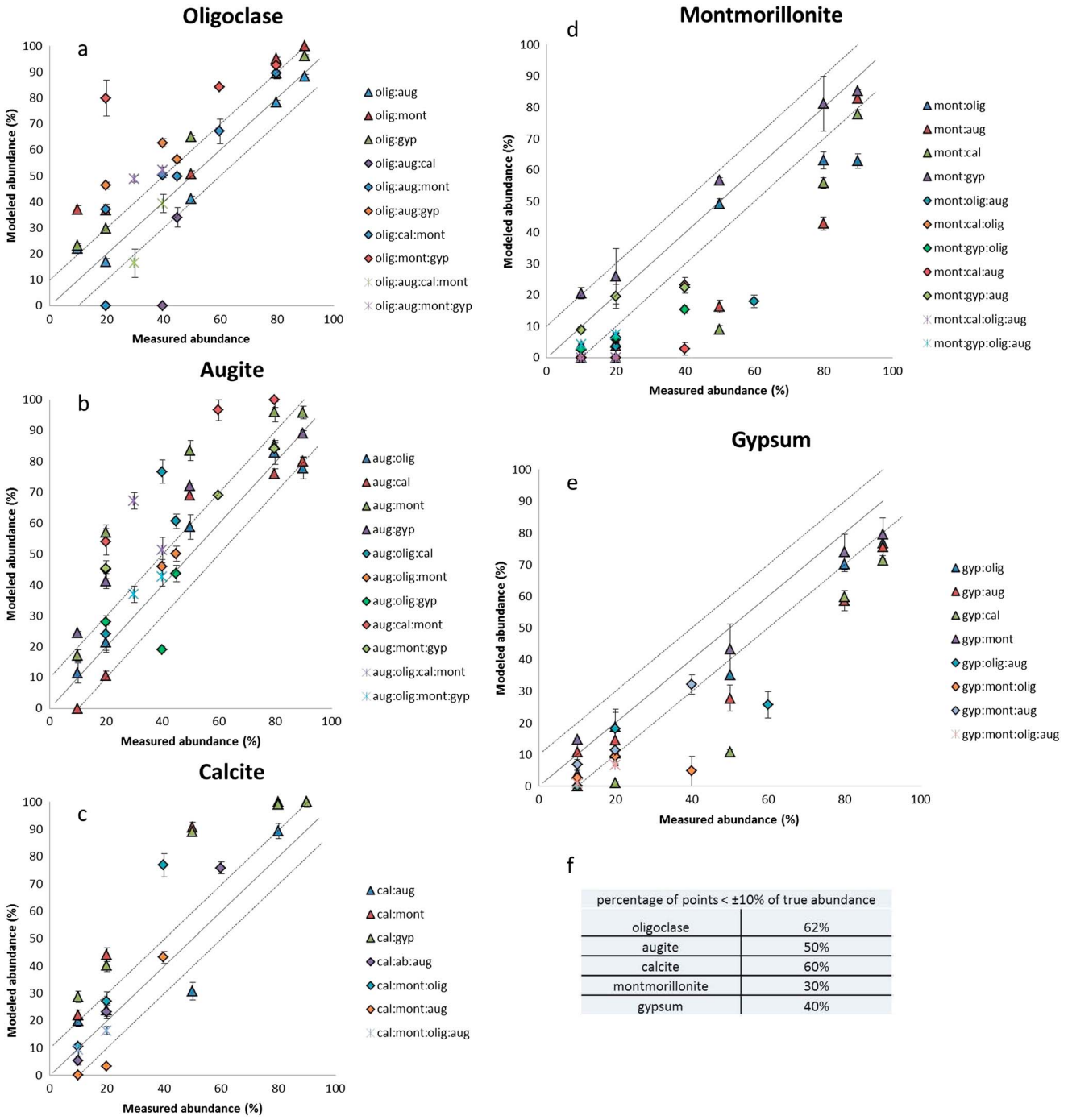

f

percentage of points < ±10% of true abundance	
oligoclase	62%
augite	50%
calcite	60%
montmorillonite	30%
gypsum	40%

Figure 5. Measured abundance and modeled abundance derived from NNLS for (a) oligoclase, (b) augite, (c) calcite, (d) montmorillonite, and (e) gypsum and (f) percentage of points < ±10% of true abundance. The solid line represents a perfect correspondence between known abundance and NNLS modeled abundance, and the dashed lines are ±10% from the 1:1 correspondence line. The error bars are statistical errors from NNLS [*Rogers and Aharonson*, 2008].

as some of the other frequencies described above. Despite the lack of clear correspondence between regression coefficient values and emissivity features, the coefficients accurately predict the abundance of oligoclase, with more than 84% of the modeled oligoclase abundances falling within ±10% of the known abundance (Figure 7a). False positives were observed for some nonoligoclase-bearing mixtures; these most commonly occurred in montmorillonite-bearing mixtures, and modeled abundances were generally <20% (Table S2).

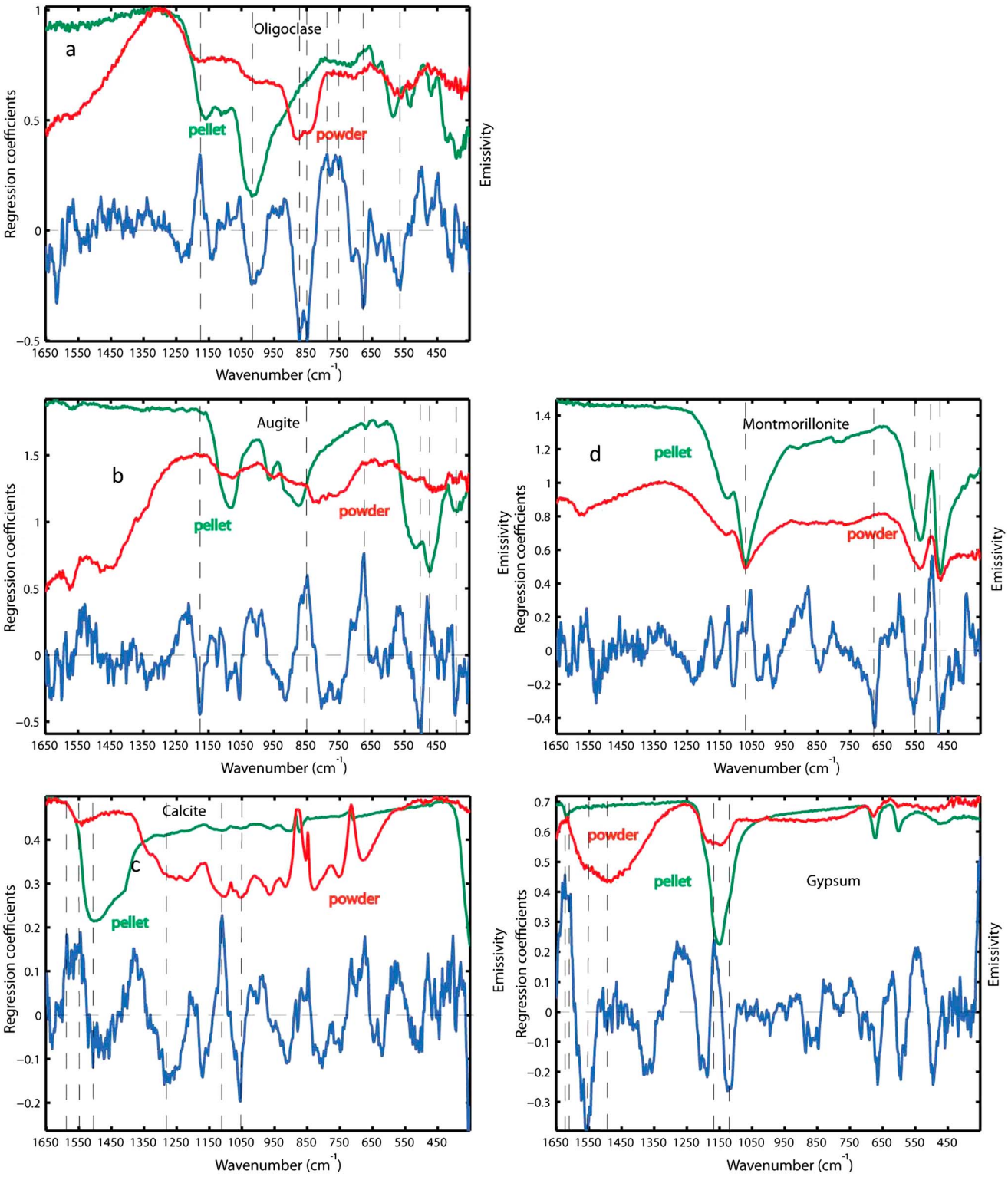

Figure 6. Regression coefficients derived from PLS for (a) oligoclase, (b) augite, (c) calcite, (d) montmorillonite, and (e) gypsum. The blue lines are regression coefficients for each mineral. Spectra of single phases were plotted for comparison and offset for clarity. No scaling or offset factors were applied for regression coefficients. Vertical dashed lines indicate the strongest regression coefficients and/or other features discussed in the text. Vertical dash lines are strongest regression coefficients and emissivity absorption features. Horizontal lines are zero reference for regression coefficients.

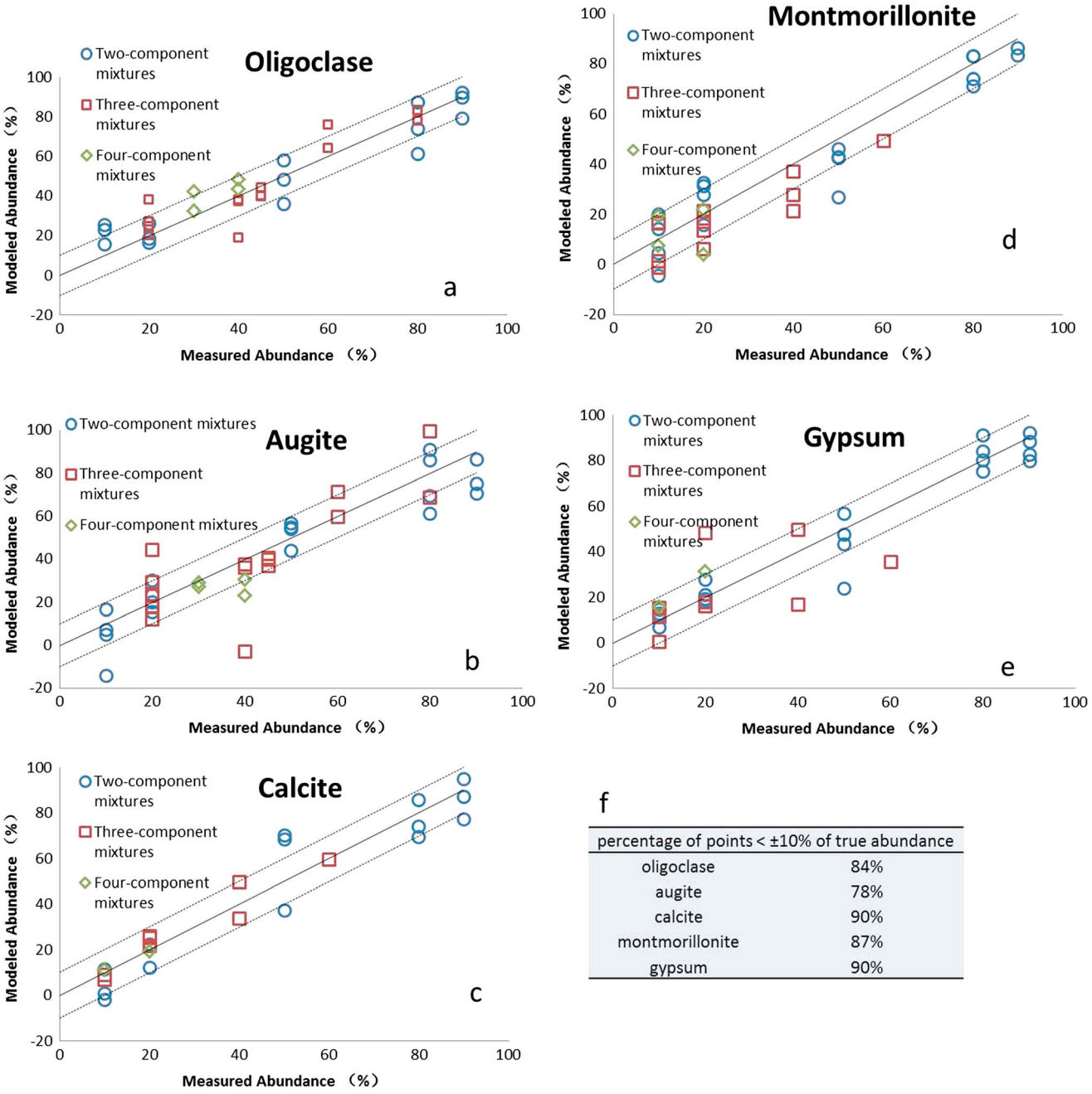

f

percentage of points < ±10% of true abundance	
oligoclase	84%
augite	78%
calcite	90%
montmorillonite	87%
gypsum	90%

Figure 7. Measured abundance and modeled abundance derived from PLS for (a) oligoclase, (b) augite, (c) calcite, (d) montmorillonite, and (e) gypsum (f) and percentage of points < ±10% of true abundance. The solid line represents a perfect correspondence between known abundance and PLS modeled abundance, and the dashed lines are ±10% from the 1:1 correspondence line.

For augite, the strongest regression coefficients are at ~1170, 850, 670, 500, 460, and 400 cm^{-1} (Figure 6b). As with oligoclase, most of these do not correspond with the strongest emissivity absorptions or peaks. The ~1170 cm^{-1} coefficient corresponds to the Christiansen feature of augite. The ~460 cm^{-1} coefficient corresponds to the near center of a low-frequency major absorption of the augite pellet and the ~400 cm^{-1} value to a minor absorption feature of both augite powder and pellet. The ~850 cm^{-1} coefficient is colocated with the shoulder of the broad fundamental absorption, and the ~670 cm^{-1} value is not correlated with any absorption. Augite abundances for approximately 22% of the mixtures are incorrectly modeled by more than ±10% (Figure 7b). The accuracy of modeled abundance increases as the number of mixture components

increase (Figure 7b). In some mixtures where augite is not truly present, low abundances of augite (<20%) were modeled with PLS, with one mixture (oligoclase-montmorillonite-gypsum) exhibiting 45% modeled abundance of augite (Table S2). These false positives are discussed further in section 4.

For calcite, in general, the regression coefficients overall are lower than those of the other four minerals. As discussed in section 4, this is likely due to the very low degree of overlap between absorptions in the pellet and powder versions of calcite, as well as the presence of features for calcite powder occurring across much of the spectral range. Though they are generally low, the strongest regression coefficients are located near ~1590, 1550, 1280, 1010, and 1050 cm^{-1}. The ~1550, 1280, 1010, and 1050 cm^{-1} coefficients correspond to absorption features of calcite powder while the coefficient at ~1590 cm^{-1} is near the Christiansen frequency (Figure 6c). The strongest absorption feature of calcite pellet at ~1500 cm^{-1} corresponds to only a moderately strong regression coefficient compared to the other features. Modeled calcite abundances for more than 90% of the mixtures fall within the ±10% of known abundance. Modeled abundances for the remaining mixtures are generally underestimated, except for one false detection (Figure 7c). Calcite abundances from the three-component mixtures are modeled less accurately than those from two- and four-component mixtures (Figure 7c).

Montmorillonite exhibits a fewer number of strong regression coefficients, but those values are among the highest observed for all five minerals of this study. As described in section 4, this is likely due to similarities between the powdered and pellet versions of montmorillonite. Two of the strongest regression coefficients, at ~500 and 470 cm^{-1} correspond directly with the peak and valley of one half of the spectral doublet that is characteristic of dioctahedral smectite clays [*Michalski et al*., 2006; *Ruff and Christensen*, 2007] (Figure 6d). A strong coefficient at ~550 cm^{-1} corresponds to the shoulder of the higher-frequency portion of the doublet. Last, a strong coefficient at ~670 cm^{-1} is not related to any particular absorption or peak. The strong absorption feature of montmorillonite pellet and powder at ~1040 cm^{-1} corresponds to only a weak regression coefficient. Modeled montmorillonite abundances for ~13% of the mixtures fall outside ±10% of known abundance (Figure 7d). As with the calcite results, modeled montmorillonite abundances for the remaining mixtures are all generally underestimated, with a few exceptions (Figure 7d).

For gypsum, the strongest regression coefficients are at ~1600–1630, 1550, 1160, and 1130 cm^{-1}. The values in the ~1600–1630 cm^{-1} range correspond to a small bound water peak [*Salisbury et al*., 1991] in the gypsum powder, which is manifested as a minor absorption in the gypsum pellet. The other strongest coefficients correspond to the shoulders of the broad fundamental absorption centered at ~1150 cm^{-1}. Modeled gypsum abundances for more than 90% of the mixtures fall within ±10% of known abundance, with no false detections (Figure 7e). Four of the mixtures, however, exhibit modeled gypsum abundances greater than 20% from the known value.

Note that PLS has no constraint to sum to 100%; in addition, negative abundance values are permitted by the algorithm (Figure 7 and Table S2). In our results, negative values are usually between 0 and −5%. Small negative values likely arise from subtle, nonsystematic differences in slope between samples. The slight differences in spectral slope can arise from variable temperatures in the field of view during the measurement. This would result in overestimate or underestimate of one component, resulting in compensation using negative abundances of other components.

3.2. Mudstone Samples

Figure 8 compares NNLS-derived mineral abundances with PLS-derived abundances to that of XRD abundances for the mudstone samples from paper 1 [*Thorpe et al*., 2015]. The PLS method retrieved known abundances to within ±10% for the majority of the mudstones, with no more than three samples falling outside this range. Modeled mica abundances are significantly improved using the PLS method. For the remaining three mineral groups, model accuracy from PLS and NNLS is comparable, with perhaps slightly better accuracy for PLS on quartz and clay abundances (Figure 8).

4. Discussion

4.1. Spectral Characteristics of Compacted Fine-Grained Particulates

Figure 1 demonstrates that the spectral characteristics of compacted fine grains exhibit nonnegligible differences from coarse-grained sands of identical composition. Compared to sand samples, compressed powders

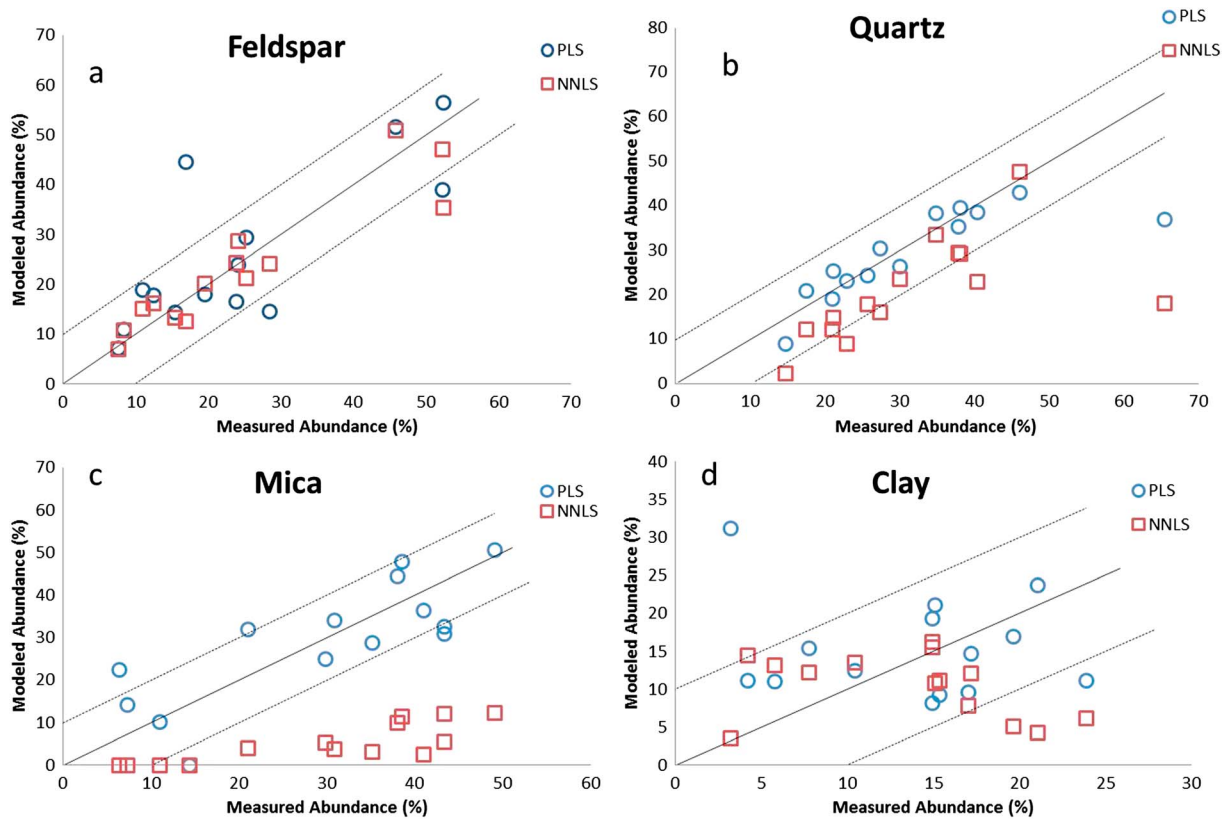

Figure 8. Measured XRD abundances and modeled abundance derived from PLS for (a) feldspar, (b) quartz, (c) mica, (d) and clays for mudstone samples. Modeled abundance derived from NNLS was plotted for comparison. The solid line represents a perfect correspondence between known abundance and modeled abundance, and the dashed lines are ±10% from the 1:1 correspondence line.

show reduced spectral contrast and shifts in the position of some absorption features. As described in section 1, this is to be expected given that both surface and volume scattering occur within a particulate medium [*Hunt and Vincent*, 1968; *Salisbury and Eastes*, 1985; *Salisbury and Wald*, 1992]. Compaction of the fine particles minimizes (or eliminates) the multiple surface reflections, but some amount of the volume scattered component remains [*Salisbury and Wald*, 1992]. Because the magnitude of k is wavelength-dependent, spectral changes due to transmission through small grains and multiple reflections in the volume are only observed across portions of the spectrum.

4.2. Applicability of NNLS to Compacted Fine-Grained Mixtures

Compared to coarse-grained ($\gtrsim$60 μm) particulate mixtures and rocks [*Ramsey and Christensen*, 1998; *Feely and Christensen*, 1999; paper 1], the accuracy of the NNLS model is poor for compacted fine-grained mixtures (Figure 5). Though many of the modeled abundances are within ±10% of the known abundance, approximately 40–70% were not, depending on which minerals were present in each combination. For oligoclase, augite, and calcite, the modeled abundances are overestimated in most of the cases, whereas for montmorillonite and gypsum, the modeled abundances are generally underestimated.

Clues to the cause(s) of the poor performance of NNLS come from Figure 1, which shows noticeable spectral changes between pressed fine grains and coarse-grained sands of the same composition. This suggests that transmission through small grains is occurring over portions of the wavelength range, due to small absorption coefficients in those ranges. In addition, the larger number of grains per volume results in multiple reflections in the volume (section 4.1). With mixtures, these volume scattering effects would result in a disproportionate number of photon interactions with the more strongly absorbing phases (which varies as a function of wavelength) and thus reduces the ability to model abundances accurately with NNLS.

Over portions of the spectral range, however, the features scale predictably with abundance. For example, in the oligoclase-augite binary mixture (Figure 2), an augite fundamental feature near ~1070 cm^{-1} decreases in strength with decreasing abundance and is replaced by an oligoclase peak at that location. In another example, using the gypsum-oligoclase binary mixture (Figure S2), the gypsum Restrahlen band decreases with gypsum abundance, and the oligoclase fundamental feature near 1010 cm^{-1} begins to appear. These examples indicate that volume scattering is not significant for the entire wavelength range for many of the mixtures. However, because NNLS treats each channel equally, it is unable to produce a linear combination across the entire wavelength range used for modeling.

4.3. Applicability of PLS to Compacted Fine-Grained Mixtures

The PLS method was able to accurately recover the known abundances (to within ±10%) for 78–90% our synthetic mixtures and for 85 % of the mudstone samples. This is in contrast to model accuracies found by a similar study investigating a lunar sample [*Li et al*., 2012], in which PLS was applied to visible/near-infrared (VNIR) spectra of mineral mixtures. We suggest that the difference in applicability findings are due to the higher k values that are typically found in the TIR range; because k is usually very high (>1) over some portion of the TIR, combinations are linear (or close to linear) over portions of the range. However, in the VNIR, the low k values (usually $\lesssim 10^{-2}$) across the full wavelength range results in nonlinear combinations across that range. In that situation, PLS cannot be used to retrieve accurate abundances.

Despite the excellent agreement between known and modeled abundances for most of our mixtures, there are a few issues worthy of discussion. First, false positive detections were observed for some minerals (for example, section 3.1.2). We suggest that this is likely due to overlap in the wavelength locations of strong regression coefficients for some of our minerals. For example, PLS identified a moderately strong regression coefficient at ~550 cm^{-1} and ~660 cm^{-1} for both oligoclase and montmorillonite. Correspondingly, oligoclase was identified at low levels in montmorillonite-bearing mixtures, even where oligoclase was absent. Second, the regression coefficients derived from some of our mixtures are relatively low compared to others. For example, regression coefficients derived for calcite are much lower than those derived from montmorillonite. This is likely due to the grouping of both powders and pellet samples in the training set; the drastically different absorption features in different wavelength ranges between powders and pellets may result in less of a correlation and lower regression coefficients for a single calcite "group." The regression coefficients are indicators of the importance of each wavelength for predicting the abundance within the system from which they were derived. The importance of a particular wavelength for a given mineral may be obscured or diluted if the absorption features for powders and pellets are in different locations. In future work, a potential way to overcome this would be to treat these as subgroups for a given mineral and combine abundances for each subgroup. Third, the strongest regression coefficients are sometimes correlated with a strong emissivity absorption but in other cases are not; this varies from mineral to mineral. For example, the regression coefficients for montmorillonite at ~470 and 500 cm^{-1} are correlated to strong absorption features of montmorillonite, but most of the coefficients for augite are not correlated to strong emissivity features of augite. A similar phenomenon was described for Induced Breakdown Spectroscopy (LIBS) data [*Dyar et al*., 2012], where the strongest regression coefficients were sometimes associated with the weaker atomic emission lines. As described above, one possible explanation is that the spectral shapes of powder and pellet for montmorillonite are similar, whereas for augite, they are different. However, this is also strongly controlled by the spectral characteristics of all other components in the training set. For example, for a given mineral whose major absorptions overlap fully or partially with another mineral, the shoulder of a feature or the absence of a feature may prove to be the strongest drivers of the coefficients for that mineral.

In summary, all of these issues can be generally attributed to the appropriateness of the training set; thus, the training set is the key to model accuracy of PLS. This can include not only adding mixtures of additional varying proportions but also deleting nonrelevant mixtures from the training set.

PLS offers many advantages over NNLS but like any technique also has its limitations. The major advantage of PLS is improved accuracy for fine-grained compacted mixtures (compare Figures 5 and 7). In addition, PLS allows an unlimited number of samples in the training data set. In contrast, NNLS requires that the number of library spectra be less than or equal to the number of channels in the mixed spectrum. A third advantage is the ability to retrieve mineral abundances without a complete library of isolated, pure end-members. This could prove useful in cases where rocks contain phases that are difficult to isolate for spectral measurement;

example phases include pigeonite [*Hamilton and Christensen*, 2000] and sericite (paper 1), which are underrepresented or absent from spectral libraries. As long as these phases can be quantified in the training set through other techniques (e.g., XRD and petrographic imaging), it should be possible to retrieve their abundance from the mixed spectrum of interest despite absence of spectral library data. The biggest practical limitation of PLS is the need to first develop a well-characterized training set of relevant mixtures. This requires either preparation of numerous synthetic mixtures and/or characterization of natural samples through independent quantitative techniques (e.g., XRD and petrographic imaging). A second limitation of PLS applied to TIR spectra is that like NNLS, abundances cannot be retrieved for minerals that are spectrally transparent across much of the wavelength range, such as chlorides (e.g., [*Lane and Christensen*, 1998; *Baldridge et al*., 2004]). Last, as with NNLS, differences in spectral contrast within the training set, such as those that might arise if spectra of both coarse particulate mixtures and rocks are included, can affect the derived abundances from PLS (supporting information Text S1). Ideal training sets for PLS would include spectra from samples of similar particle size or similar compaction. An exception to this would be the inclusion of samples which have unique features due to their particle size (for example, fine powders, which have transparency features that are not observable in coarse-grained samples).

Though not investigated in this study, PLS might be applicable to *noncompacted* fine-grained ($<$60 μm) mixtures or to coated rocks, provided some portions of the wavelength range were dominated by surface reflections. For some noncompacted mixtures of only a few components, it is possible that this condition could be met. This is an area deserving more attention in future studies.

4.4. Implications for Mineral Abundance Estimation on Martian Surfaces

Results from our study indicate that the NNLS modeled abundances of clays, in compacted fine-grained ($<$10–25 μm) mixtures are commonly underestimated. This differs somewhat from previous results using natural mudstones [*Michalski et al*., 2006; *Thorpe et al*., 2015], where clay abundances were commonly predicted to be within 10% of the known or, in some cases, slightly overestimated [*Michalski et al*., 2006]. The differences may be related to differences in the host matrix (e.g., what other minerals are present in the mixtures, such as augite) or perhaps differences in bulk grain size. In any case, the possibility of underestimating clay abundances in fine-grained compacted mixtures is relevant to interpreting mineral abundances from known phyllosilicate-bearing regions from the higher spatial resolution NIR imaging spectrometers Compact Reconnaissance Imaging Spectrometer for Mars and Observatoire pour la Minéralogie, l'Eau, les Glaces et l'Activité (OMEGA). For example, from radiative transfer modeling of OMEGA NIR spectra, select regions of Mawrth Vallis exhibit modeled abundances as high as 65%; modeled abundances are as high as 35% in other locations in the southern highlands [*Poulet et al*., 2008]. However, conventional linear least squares models of TES spectra show less than 15% of phyllosilicate at Mawrth Vallis and ~30% or less in the southern highlands [*McDowell and Hamilton*, 2009; *Michalski and Fergason*, 2009; *Michalski et al*., 2010]. Though differences in spatial resolution are likely major contributors to these discrepancies, spatial resolution cannot fully account for the differences [*Viviano and Moersch*, 2013]. Our results demonstrate that clay abundances in some fine-grained compacted mixtures could be underestimated by ~10–40% in linear least squares models of TIR spectra.

More broadly, our study indicates that TIR spectra from very fine grained sedimentary rocks (e.g., $<$~10 μm) cannot be modeled reliably with the conventional least squares methods [*Ramsey and Christensen*, 1998; *Rogers and Aharonson*, 2008]. But PLS can be used to recover abundances from very fine grained rocks to within ±10% (absolute) from TIR data sets, provided a suitable training set is available. Mini-TES observations of fine-grained rocks at Gusev crater and Meridiani Planum [*Christensen et al*., 2004a, 2004b; *Grotzinger et al*., 2005; *McLennan et al*., 2005] could be ideal data sets in which to apply PLS. PLS could also potentially be applied to orbital observations, provided atmospheric components were first removed (e.g., [*Bandfield and Smith*, 2003]). Low-dust sedimentary deposits hosting phyllosilicates such as Mawrth Vallis, Jezero crater, and Eberswalde crater [*Ehlmann et al*., 2008a; *Murchie et al*., 2009; *Dehouck et al*., 2010; *Milliken and Bish*, 2010; *Milliken et al*., 2010; *Ansan et al*., 2011; *Wray et al*., 2011] would be ideal for analyzing mineral abundance with PLS, due to the likely mixture of both coarse and fine grains.

5. Conclusions

We characterized the thermal infrared spectral properties of compacted, very fine grained ($<$10 μm) mineral mixtures of oligoclase, augite, calcite, montmorillonite, and gypsum. Nonnegative linear least squares

minimization (NNLS) using spectra of pellets and powders of the end-member minerals was used to assess the linearity of spectral combination of fine-grained mixtures, by modeling mineral abundance of mixtures over the 350–1650 cm^{-1} spectral range. For the first time, we also applied a partial least squares (PLS) model to thermal emission spectra of synthetic mixtures and natural mudstones to assess its applicability for retrieving mineral abundances from to fine-grained rocks. We have made the following major observations and conclusions:

1. Notable differences between thermal infrared spectra of the sand and compacted powder (pellet) versions of minerals are present, both in terms of spectral contrast and spectral shape. These differences are likely due to an increased contribution of volume scattering in the compacted fine-grained material relative to that in the larger, optically thick sand grains (section 4.1).
2. The NNLS modeled abundances for all five minerals investigated are within ±10% of the known abundances for 39% of the mixtures. Model accuracy varies depending on the mineral and also on other mixture components (Figure 5). For oligoclase, augite, and calcite, the modeled abundances are overestimated in most of the cases, whereas for montmorillonite and gypsum, the modeled abundances are generally underestimated. However, these trends depend greatly on other components present in the mixture and cannot be universally applied (section 4.4). Results show that the relationships between known and modeled abundance follow nonlinear curves. Drawing from the literature, we suggest that the poor performance of NNLS is due to a combination of transmission through small grains over portions of the wavelength range and multiple photon reflections in the volume.
3. The PLS method was able to accurately recover the known abundances (to within ±10%) for 78–90% of our synthetic mixtures. We suggest that the excellent agreement between known and modeled abundances is due to the higher *k* values that are typically found in the TIR range; because *k* is usually very high (>1) over some portion of the TIR range, combinations are linear over portions of the range.
4. The PLS method retrieved known abundances to within ±10% for 85% of the mudstone samples, with no more than 3 out of 14 samples falling outside this range. Modeled mica abundances are significantly improved using the PLS method, compared to NNLS.
5. Our study indicates that thermal infrared spectra from very fine grained ($<10\,\mu m$) rocks cannot be modeled reliably with NNLS. But PLS can be used to recover abundances from very fine grained rocks to within ±10% (absolute) from TIR data sets, provided a suitable training set is available. PLS could also potentially be applied to orbital observations, provided atmospheric components were first removed.

Acknowledgments

We thank Jacob Gardner and Kaitlin McIntosh for their assistance with the sample preparation. We are grateful to Jun Huang and Christina Viviano-Beck for their thorough and constructive reviews, which greatly improved this manuscript. We acknowledge funding from the NASA Mars Fundamental Research Program grant NNX09AL22G to A.D. Rogers. All spectral data presented in this work are available in Table form in the supporting information and are also available upon request from the authors.

References

Ansan, V., et al. (2011), Stratigraphy, mineralogy, and origin of layered deposits inside Terby crater, Mars, *Icarus*, *211*(1), 273–304, doi:10.1016/j.icarus.2010.09.011.

Baldridge, A. M., and P. R. Christensen (2009), A laboratory technique for thermal emission measurement of hydrated minerals, *Appl. Spectrosc.*, *63*(6), 678–688.

Baldridge, A. M., J. D. Farmer, and J. E. Moersch (2004), Mars remote-sensing analog studies in the Badwater Basin, Death Valley, California, *J. Geophys. Res.*, *109*, E12006, doi:10.1029/2004JE002315.

Bandfield, J. L. (2002), Global mineral distributions on Mars, *J. Geophys. Res.*, *107*(E6), 5042, doi:10.1029/2001JE001510.

Bandfield, J. L., and M. D. Smith (2003), Multiple emission angle surface-atmosphere separations of Thermal Emission Spectrometer data, *Icarus*, *161*(1), 47–65, doi:10.1016/s0019-1035(02)00025-8.

Bandfield, J. L., T. D. Glotch, and P. R. Christensen (2003), Spectroscopic identification of carbonate minerals in the martian dust, *Science*, *301*(5636), 1084–1087, doi:10.1126/science.1088054.

Boynton, W. V., et al. (2009), Evidence for calcium carbonate at the Mars Phoenix Landing Site, *Science*, *325*(5936), 61–64, doi:10.1126/science.1172768.

Carter, J., F. Poulet, J. P. Bibring, N. Mangold, and S. Murchie (2013), Hydrous minerals on Mars as seen by the CRISM and OMEGA imaging spectrometers: Updated global view, *J. Geophys. Res. Planets*, *118*, 831–858, doi:10.1029/2012JE004145.

Chipera, S. J., and D. L. Bish (2001), Baseline studies of the clay minerals society source clays: Powder X-ray diffraction analyses, *Clays Clay Miner.*, *49*(5), 398–409, doi:10.1346/ccmn.2001.0490507.

Christensen, P. R., et al. (2000a), Detection of crystalline hematite mineralization on Mars by the Thermal Emission Spectrometer: Evidence for near-surface water, *J. Geophys. Res.*, *105*(E4), 9623–9642, doi:10.1029/1999JE001093.

Christensen, P. R., J. L. Bandfield, M. D. Smith, V. E. Hamilton, and R. N. Clark (2000b), Identification of a basaltic component on the Martian surface from Thermal Emission Spectrometer data, *J. Geophys. Res.*, *105*(E4), 9609–9621, doi:10.1029/1999JE001127.

Christensen, P. R., et al. (2001), Mars Global Surveyor Thermal Emission Spectrometer experiment: Investigation description and surface science results, *J. Geophys. Res.*, *106*(E10), 23,823–23,871, doi:10.1029/2000JE001370.

Christensen, P. R., et al. (2003), Morphology and composition of the surface of Mars: Mars Odyssey THEMIS results, *Science*, *300*(5628), 2056–2061, doi:10.1126/science.1080885.

Christensen, P. R., et al. (2004a), Initial results from the Mini-TES experiment in Gusev crater from the Spirit rover, *Science*, *305*(5685), 837–842, doi:10.1126/science.1100564.

Christensen, P. R., et al. (2004b), Mineralogy at Meridiani Planum from the Mini-TES experiment on the Opportunity rover, *Science*, *306*(5702), 1733–1739, doi:10.1126/science.1104909.

Clark, R. N., and T. L. Roush (1984), Reflectance spectroscopy: Quantitative analysis techniques for remote-sensing applications, *J. Geophys. Res.*, *89*(NB7), 6329–6340, doi:10.1029/JB089iB07p06329.
Clegg, S. M., E. Sklute, M. D. Dyar, J. E. Barefield, and R. C. Wiens (2009), Multivariate analysis of remote laser-induced breakdown spectroscopy spectra using partial least squares, principal component analysis, and related techniques, *Spectrochim. Acta, Part B*, *64*(1), 79–88, doi:10.1016/j.sab.2008.10.045.
Cooper, C. D., and J. F. Mustard (2002), Spectroscopy of loose and cemented sulfate-bearing soils: Implications for duricrust on Mars, *Icarus*, *158*(1), 42–55, doi:10.1006/icar.2002.6874.
Dehouck, E., N. Mangold, S. Le Mouelic, V. Ansan, and F. Poulet (2010), Ismenius Cavus, Mars: A deep paleolake with phyllosilicate deposits, *Planet. Space Sci.*, *58*(6), 941–946, doi:10.1016/j.pss.2010.02.005.
Dobrea, E. Z. N., et al. (2010), Mineralogy and stratigraphy of phyllosilicate-bearing and dark mantling units in the greater Mawrth Vallis/west Arabia Terra area: Constraints on geological origin, *J. Geophys. Res.*, *115*, E00D19, doi:10.1029/2009JE003351.
Dyar, M. D., M. L. Carmosino, E. A. Breves, M. V. Ozanne, S. M. Clegg, and R. C. Wiens (2012), Comparison of partial least squares and lasso regression techniques as applied to laser-induced breakdown spectroscopy of geological samples, *Spectrochim. Acta, Part B*, *70*, 51–67, doi:10.1016/j.sab.2012.04.011.
Ehlmann, B. L., J. F. Mustard, C. I. Fassett, S. C. Schon, J. W. Head, D. J. D. Marais, J. A. Grant, and S. L. Murchie (2008a), Clay minerals in delta deposits and organic preservation potential on Mars, *Nat. Geosci.*, *1*(6), 355–358, doi:10.1038/ngeo207.
Ehlmann, B. L., et al. (2008b), Orbital identification of carbonate-bearing rocks on Mars, *Science*, *322*(5909), 1828–1832, doi:10.1126/science.1164759.
Ehlmann, B. L., J. F. Mustard, S. L. Murchie, J. P. Bibring, A. Meunier, A. A. Fraeman, and Y. Langevin (2011), Subsurface water and clay mineral formation during the early history of Mars, *Nature*, *479*(7371), 53–60, doi:10.1038/nature10582.
Farmer, V. C. (1974), The layer silicates, in *Infrared Spectra of Minerals*, pp. 331–363, Mineral. Soc., London.
Feely, K. C., and P. R. Christensen (1999), Quantitative compositional analysis using thermal emission spectroscopy: Application to igneous and metamorphic rocks, *J. Geophys. Res.*, *104*(E10), 24,195–24,210, doi:10.1029/1999JE001034.
Glotch, T. D., J. L. Bandfield, P. R. Christensen, W. M. Calvin, S. M. McLennan, B. C. Clark, A. D. Rogers, and S. W. Squyres (2006), Mineralogy of the light-toned outcrop at Meridiani Planum as seen by the Miniature Thermal Emission Spectrometer and implications for its formation, *J. Geophys. Res.*, *111*, E12S03, doi:10.1029/2005JE002672.
Grotzinger, J. P., and R. E. Milliken (2012), The sedimentary rock record of mars: Distribution, origins, and global stratigraphy, in *Sedimentary Geology of Mars*, edited by J. P. Grotzinger and R. E. Milliken, pp. 1–48, SEPM Soc. for Sediment., Tulsa Okla.
Grotzinger, J. P., et al. (2005), Stratigraphy and sedimentology of a dry to wet eolian depositional system, Burns formation, Meridiani Planum, Mars, *Earth Planet. Sci. Lett.*, *240*(1), 11–72, doi:10.1016/j.epsl.2005.09.039.
Grotzinger, J. P., et al. (2014), A habitable fluvio-lacustrine environment at Yellowknife Bay, Gale Crater, Mars, *Science*, *343*(6169), 14, doi:10.1126/science.1242777.
Hamilton, V. E., and P. R. Christensen (2000), Determining the modal mineralogy of mafic and ultramafic igneous rocks using thermal emission spectroscopy, *J. Geophys. Res.*, *105*(E4), 9717–9733, doi:10.1029/1999JE001113.
Hamilton, V. E., and S. W. Ruff (2012), Distribution and characteristics of Adirondack-class basalt as observed by Mini-TES in Gusev crater, Mars and its possible volcanic source, *Icarus*, *218*(2), 917–949, doi:10.1016/j.icarus.2012.01.011.
Hapke, B. (1993), *Introduction to the Theory of Reflectance and Emittance Spectroscopy*, Cambridge Univ. Press, New York.
Hecker, C., J. H. Dilles, M. van der Meijde, and F. D. van der Meer (2012), Thermal infrared spectroscopy and partial least squares regression to determine mineral modes of granitoid rocks, *Geochem. Geophys. Geosyst.*, *13*, Q03021, doi:10.1029/2011GC004004.
Hook, S. J., J. E. Dmochowski, K. A. Howard, L. C. Rowan, K. E. Karlstrom, and J. M. Stock (2005), Mapping variations in weight percent silica measured from multispectral thermal infrared imagery—Examples from the Hiller Mountains, Nevada, USA and Tres Virgenes-La Reforma, Baja California Sur, Mexico, *Remote Sens. Environ.*, *95*(3), 273–289, doi:10.1016/j.rse.2004.11.020.
Huang, J., and L. Xiao (2014), Compositional evolution of lava plains in the Syria-Thaumasia Block, Mars, *Sci. China: Phys., Mech. Astron.*, *57*(5), 994–1000, doi:10.1007/s11433-014-5407-3.
Hunt, G. R., and L. M. Logan (1972), Variation of single-particle mid-infrared emission-spectrum with particle-size, *Appl. Opt.*, *11*(1), 142–147, doi:10.1364/ao.11.000142.
Hunt, G. R., and R. K. Vincent (1968), The behavior of spectral features in the infrared emission from particulate surfaces of various grain sizes, *J. Geophys. Res.*, *73*(18), 6039–6046, doi:10.1029/JB073i018p06039.
Jackson, M. L. (1967), *Soil Chemical Analysis*, pp. 146–157, Prentice Hall of India, New Delhi, India.
Kahle, A. B., M. S. Shumate, and D. B. Nash (1984), Active airborne infrared-laser system for identification of surface rock and minerals, *Geophys. Res. Lett.*, *11*(11), 1149–1152, doi:10.1029/GL011i011p01149.
Koeppen, W. C., and V. E. Hamilton (2008), Global distribution, composition, and abundance of olivine on the surface of Mars from thermal infrared data, *J. Geophys. Res.*, *113*, E05001, doi:10.1029/2007JE002984.
Kruse, F., A. Lefkoff, J. Boardman, K. Heidebrecht, A. Shapiro, P. Barloon, and A. Goetz (1993), The spectral image processing system (SIPS)—interactive visualization and analysis of imaging spectrometer data, *Remote Sens. Environ.*, *44*(2–3), 145–163.
Lane, M. D. (2007), Mid-infrared emission spectroscopy of sulfate and sulfate-bearing minerals, *Am. Mineral.*, *92*(1), 1–18, doi:10.2138/am.2007.2170.
Lane, M. D., and P. R. Christensen (1997), Thermal infrared emission spectroscopy of anhydrous carbonates, *J. Geophys. Res.*, *102*(E11), 25,581–25,592, doi:10.1029/97JE02046.
Lane, M. D., and P. R. Christensen (1998), Thermal infrared emission spectroscopy of salt minerals predicted for Mars, *Icarus*, *135*(2), 528–536, doi:10.1006/icar.1998.5998.
Lawson, C. L., and R. J. Hanson (1974), *Solving Least Squares Problems*, Society for Industrial and Applied Mathematics (SIAM), Englewood Cliffs, N. J., doi:10.1137/1.9781611971217.
Li, S., L. Li, R. Milliken, and K. Song (2012), Hybridization of partial least squares and neural network models for quantifying lunar surface minerals, *Icarus*, *221*(1), 208–225, doi:10.1016/j.icarus.2012.07.023.
Lucey, P. G. (2004), Mineral maps of the Moon, *Geophys. Res. Lett.*, *31*, L08701, doi:10.1029/2003GL019406.
Lyon, R. (1965), Analysis of rocks by spectral infrared emission (8 to 25 microns), *Econ. Geol.*, *60*(4), 715–736.
Malin, M. C., and K. S. Edgett (2000), Sedimentary rocks of early Mars, *Science*, *290*(5498), 1927–1937, doi:10.1126/science.290.5498.1927.
McDowell, M. L., and V. E. Hamilton (2009), Seeking phyllosilicates in thermal infrared data: A laboratory and Martian data case study, *J. Geophys. Res.*, *114*, E06007, doi:10.1029/2008JE003317.
McLennan, S. M., et al. (2005), Provenance and diagenesis of the evaporite-bearing Burns formation, Meridiani Planum, Mars, *Earth Planet. Sci. Lett.*, *240*(1), 95–121, doi:10.1016/j.epsl.2005.09.041.
McLennan, S. M., et al. (2014), Elemental geochemistry of sedimentary rocks at Yellowknife Bay, Gale crater, Mars, *Science*, *343*(6169), 10, doi:10.1126/science.1244734.

Michalski, J. R., and R. L. Fergason (2009), Composition and thermal inertia of the Mawrth Vallis region of Mars from TES and THEMIS data, *Icarus*, *199*(1), 25–48, doi:10.1016/j.icarus.2008.08.016.
Michalski, J. R., and P. B. Niles (2010), Deep crustal carbonate rocks exposed by meteor impact on Mars, *Nat. Geosci.*, *3*(11), 751–755, doi:10.1038/NGEO971.
Michalski, J. R., M. D. Kraft, T. G. Sharp, L. B. Williams, and P. R. Christensen (2006), Emission spectroscopy of clay minerals and evidence for poorly crystalline aluminosilicates on Mars from Thermal Emission Spectrometer data, *J. Geophys. Res.*, *111*, E03004, doi:10.1029/2005JE002438.
Michalski, J. R., F. Poulet, J. P. Bibring, and N. Mangold (2010), Analysis of phyllosilicate deposits in the Nili Fossae region of Mars: Comparison of TES and OMEGA data, *Icarus*, *206*(1), 269–289, doi:10.1016/j.icarus.2009.09.006.
Milliken, R. E., and D. L. Bish (2010), Sources and sinks of clay minerals on Mars, *Philos. Mag.*, *90*(17–18), 2293–2308, doi:10.1080/14786430903575132.
Milliken, R. E., J. P. Grotzinger, and B. J. Thomson (2010), Paleoclimate of Mars as captured by the stratigraphic record in Gale Crater, *Geophys. Res. Lett.*, *37*, L04201, doi:10.1029/2009GL041870.
Moersch, J. E., and P. R. Christensen (1995), Thermal emission from particulate surfaces—a comparison of scattering models with measured spectra, *J. Geophys. Res.*, *100*(E4), 7465–7477, doi:10.1029/94JE03330.
Moore, D. M., and R. C. Reynolds (1997), *X-ray Diffraction and the Identification and Analysis of Clay Minerals*, 2nd ed., Oxford Univ. Press, Oxford, New York.
Murchie, S. L., J. F. Mustard, B. L. Ehlmann, R. E. Milliken, J. L. Bishop, N. K. McKeown, E. Z. Noe Dobrea, F. P. Seelos, D. L. Buczkowski, and S. M. Wiseman (2009), A synthesis of Martian aqueous mineralogy after 1 Mars year of observations from the Mars Reconnaissance Orbiter, *J. Geophys. Res.*, *114*, E00D06, doi:10.1029/2009JE003342.
Mustard, J. F., and J. E. Hays (1997), Effects of hyperfine particles on reflectance spectra from 0.3 to 25 μm, *Icarus*, *125*(1), 145–163, doi:10.1006/icar.1996.5583.
Mustard, J. F., B. L. Ehlmann, S. L. Murchie, F. Poulet, N. Mangold, J. W. Head, J. P. Bibring, and L. H. Roach (2009), Composition, morphology, and stratigraphy of Noachian Crust around the Isidis basin, *J. Geophys. Res.*, *114*, doi:10.1029/2009JE003349.
Pan, C., A. D. Rogers, and J. R. Michalski (2015), Thermal and near-infrared analyses of central peaks of Martian impact craters: Evidence for a heterogeneous Martian crust, *J. Geophys. Res. Planets*, *120*, 662–688, doi:10.1002/2014JE004676.
Poulet, F., J. P. Bibring, J. F. Mustard, A. Gendrin, N. Mangold, Y. Langevin, R. E. Arvidson, B. Gondet, C. Gomez, and T. Omega (2005), Phyllosilicates on Mars and implications for early martian climate, *Nature*, *438*(7068), 623–627, doi:10.1038/nature04274.
Poulet, F., N. Mangold, D. Loizeau, J. P. Bibring, Y. Langevin, J. Michalski, and B. Gondet (2008), Abundance of minerals in the phyllosilicate-rich units on Mars, *Astron. Astrophys.*, *487*(2), L41–U193, doi:10.1051/0004-6361:200810150.
Ramsey, M. S., and P. R. Christensen (1998), Mineral abundance determination: Quantitative deconvolution of thermal emission spectra, *J. Geophys. Res.*, *103*(B1), 577–596, doi:10.1029/97JB02784.
Roach, L. H., J. F. Mustard, G. Swayze, R. E. Milliken, J. L. Bishop, S. L. Murchie, and K. Lichtenberg (2010), Hydrated mineral stratigraphy of Ius Chasma, Valles Marineris, *Icarus*, *206*(1), 253–268, doi:10.1016/j.icarus.2009.09.003.
Rogers, A. D., and O. Aharonson (2008), Mineralogical composition of sands in Meridiani Planum determined from Mars Exploration Rover data and comparison to orbital measurements, *J. Geophys. Res.*, *113*, E06S14, doi:10.1029/2007JE002995.
Rogers, A. D., and P. R. Christensen (2007), Surface mineralogy of Martian low-albedo regions from MGS-TES data: Implications for upper crustal evolution and surface alteration, *J. Geophys. Res.*, *112*, E01003, doi:10.1029/2006JE002727.
Ruff, S. W., and P. R. Christensen (2007), Basaltic andesite, altered basalt, and a TES-based search for smectite clay minerals on Mars, *Geophys. Res. Lett.*, *34*, L10204, doi:10.1029/2007GL029602.
Ruff, S. W., P. R. Christensen, P. W. Barbera, and D. L. Anderson (1997), Quantitative thermal emission spectroscopy of minerals: A laboratory technique for measurement and calibration, *J. Geophys. Res.*, *102*(B7), 14,899–14,913, doi:10.1029/97JB00593.
Ruff, S. W., P. R. Christensen, D. L. Blaney, W. H. Farrand, J. R. Johnson, J. R. Michalski, J. E. Moersch, S. P. Wright, and S. W. Squyres (2006), The rocks of Gusev Crater as viewed by the Mini-TES instrument, *J. Geophys. Res.*, *111*, E12S18, doi:10.1029/2006JE002747.
Ruff, S. W., et al. (2011), Characteristics, distribution, origin, and significance of opaline silica observed by the Spirit rover in Gusev crater, Mars, *J. Geophys. Res.*, *116*, E00F23, doi:10.1029/2010JE003767.
Salisbury, J. W., and A. Wald (1992), The role of volume scattering in reducing spectral contrast of reststrahlen bands in spectra of powdered minerals, *Icarus*, *96*(1), 121–128, doi:10.1016/0019-1035(92)90009-v.
Salisbury, J. W., and J. W. Eastes (1985), The effect of particle-size and porosity on spectral contrast in the midinfrared, *Icarus*, *64*(3), 586–588, doi:10.1016/0019-1035(85)90078-8.
Salisbury, J. W., L. S. Walter, and N. Vergo (1987), Mid-infrared (2.1–25 mm) spectra of minerals *Rep*., U.S. Geol. Surv., Reston, Va.
Salisbury, J. W., L. S. Walter, N. Vergo, and D. M. D'Aria (1991), *Infrared (2.1–25 μm) Spectra of Minerals*, Johns Hopkins Univ. Press, Baltimore.
Smith, M. D., J. L. Bandfield, and P. R. Christensen (2000), Separation of atmospheric and surface spectral features in Mars Global Surveyor Thermal Emission Spectrometer (TES) spectra, *J. Geophys. Res.*, *105*(E4), 9589–9607, doi:10.1029/1999JE001105.
Sperazza, M., J. N. Moore, and M. S. Hendrix (2004), High-resolution particle size analysis of naturally occurring very fine-grained sediment through laser diffractometry, *J. Sediment. Res.*, *74*(5), 736–743, doi:10.1306/031104740736.
Squyres, S. W., et al. (2004), In situ evidence for an ancient aqueous environment at Meridiani Planum, Mars, *Science*, *306*(5702), 1709–1714, doi:10.1126/science.1104559.
Thorpe, M. T., A. D. Rogers, T. Bristow, and C. Pan (2015), Quantitative compositional analysis of sedimentary materials using thermal emission spectroscopy: 1. Application to sedimentary rocks, *J. Geophys. Res. Planets*, *120*, doi:10.1002/2015JE004863, in press.
Tornabene, L. L., J. E. Moersch, H. Y. McSween Jr., V. E. Hamilton, J. L. Piatek, and P. R. Christensen (2008), Surface and crater-exposed lithologic units of the Isidis Basin as mapped by coanalysis of THEMIS and TES derived data products, *J. Geophys. Res.*, *113*, E10001, doi:10.1029/2007JE002988.
Viviano, C. E., and J. E. Moersch (2013), Using THEMIS data to resolve the discrepancy between CRISM/OMEGA and TES modeled phyllosilicate abundance in Mawrth Vallis, *Icarus*, *226*(1), 497–509, doi:10.1016/j.icarus.2013.06.005.
Wold, H. (1982), Soft modelling: The basic design and some extensions, in *Systems Under Indirect Observation, Part II*, edited by K. G. Jöreskog and H. Wold, pp. 1–53, North Holland, Amsterdam.
Wold, S., M. Sjostrom, and L. Eriksson (2001), PLS-regression: A basic tool of chemometrics, *Chemom. Intell. Lab. Syst.*, *58*(2), 109–130, doi:10.1016/s0169-7439(01)00155-1.
Wray, J. J., B. L. Ehlmann, S. W. Squyres, J. F. Mustard, and R. L. Kirk (2008), Compositional stratigraphy of clay-bearing layered deposits at Mawrth Vallis, Mars, *Geophys. Res. Lett.*, *35*, L12202, doi:10.1029/2008GL034385.
Wray, J. J., et al. (2011), Columbus crater and other possible groundwater-fed paleolakes of Terra Sirenum, Mars, *J. Geophys. Res.*, *116*, 41, doi:10.1029/2010JE003694.